3D-printed phase waveplates for THz beam shaping

J. Gospodaric; A. Kuzmenko; Anna Pimenov; C. Huber; D. Suess; S. Rotter ; A. Pimenov

Check for updates

CrossMark

View Online

Export Citation

3D-printed phase waveplates for THz beam shaping

J. Gospodaric,[1] A. Kuzmenko,[1] Anna Pimenov,[1] C. Huber,[2] D. Suess,[2] S. Rotter,[3] and A. Pimenov[1]

[1]*Institute of Solid State Physics, Vienna University of Technology (TU Wien), 1040 Vienna, Austria*
[2]*Christian Doppler Laboratory for Advanced Magnetic Sensing and Materials, Faculty of Physics, University of Vienna, 1090 Vienna, Austria*
[3]*Institute for Theoretical Physics, Vienna University of Technology (TU Wien), 1040 Vienna, Austria*

The advancement of 3D-printing opens up a new way of constructing affordable custom terahertz (THz) components due to suitable printing resolution and THz transparency of polymer materials. We present a way of calculating, designing, and fabricating a THz waveplate that phase-modulates an incident THz beam ($\lambda_0 = 2.14$ mm) in order to create a predefined intensity profile of the optical wavefront on a distant image plane. Our calculations were performed for two distinct target intensities with the use of a modified Gerchberg-Saxton algorithm. The resulting phase-modulating profiles were used to model the polylactide elements, which were printed out with a commercially available 3D-printer. The results were tested in a THz experimental setup equipped with a scanning option, and they showed good agreement with theoretical predictions. *Published by AIP Publishing.*
https://doi.org/10.1063/1.5027179

Terahertz (THz) spectroscopy is a powerful tool for imaging and testing applications.[1,2] In analogy to the situation in optics, elements to manipulate the intensity and shape of a beam are of crucial importance. An efficient way to design such elements is to combine the holographic principles with computer-supported calculations of the beam propagation.[3–7] Such an approach allows not only to manipulate a beam but moreover to generate pictures of real and imaginary objects on short timescales. Recently, optical meta-surfaces[8–11] added several interesting new ideas to the field, especially on the way to miniaturize the optical units.

Alternatively, optical elements for picture generation may be produced based on phase control of light only. Such elements are often called phase holograms, and they manipulate the incident wave by coordinate-dependent phase changes.[12–16] Well-known examples of phase holograms are dielectric Fresnel lenses or dielectric diffraction gratings. All such elements can be designed for frequencies as low as terahertz because the underlying Maxwell equations of light do not contain the wavelength as a parameter.

The goal of this article is to demonstrate that a very practical way to produce such phase holograms is to work with a commercially available 3D-printer. Additive manufacturing with 3D-printers has gained significant attention in the recent years due to its versatility, accessibility, and generally because it presents a quick, easy-to-use, and cost-efficient technique to produce complex and high-precision structures. The layer height resolution of 3D-printers ($\sim$0.1 mm) and a high transparency of the polymers used in 3D-printers[17] are ideally suited for printing devices that manipulate electromagnetic radiation in the THz region. Recent examples of 3D printed THz elements are diffraction gratings, lenses, optical waveguides, prisms, etc.[18–25] Here, we make a significant further step in the field of THz imaging by designing and 3D-printing dielectric plates which are able to reproduce the picture of an arbitrary object.

In our proof-of-principle demonstration we modulate the phase profile of an incident asymmetric Gaussian beam with a wavelength of $\lambda_0 = 2.14$ mm (140 GHz) at $z_0 = 0$ mm with initially uniform zero phase profile (plane wave) in order to produce two distinct target intensity profiles [Figs. 1(a) and 1(b)] at the image plane at $z_i = 50$ mm, where the z-axis represents the optical axis. These two target profiles in the shape of a cross and of our university logo were represented on a Cartesian grid in a circular shape with a diameter of 53 mm. Equally spaced grid points were used with a nearest-neighbor distance of 0.53 mm. The incident beam was measured by scanning its intensity in the empty channel [see Fig. 2(b)] and was found to have a slightly asymmetric Gaussian profile with the widths of 13.4 and 16.6 mm along the x' and y' axes, respectively, which are rotated by 0.10 rad with respect to the x and y-axis of the optical system. These parameters were then used for calculating the profile of the phase plates explained below.

The required phase deformation of the collimated incident beam at z_0 was calculated using the Gerchberg-Saxton (GS) iterative algorithm.[26] This algorithm determines the phase of the optical wave function in the imaging system, whose intensity in the diffraction and the image plane of the system are known. The method typically assumes a Fourier transform relation between the optical fields on both planes. Therefore, in order to move the image plane from far-field to a finite distance from the diffraction plane, we considered a propagation function that linked the optical fields on both planes based on the Huygens principle. In this spirit, the wavefront on the diffraction plane at z_0, E^d, was represented as point emitters of spherical wavelets with respective coordinates (x, y), amplitude $A_{(x,y)}$, and phase angle $\varphi_{(x,y)}$. The optical field on the image plane, E^i, was then calculated by summing up all contributions from every point emitter on (x, y) for every point (x', y') of the grid on the distant image plane as
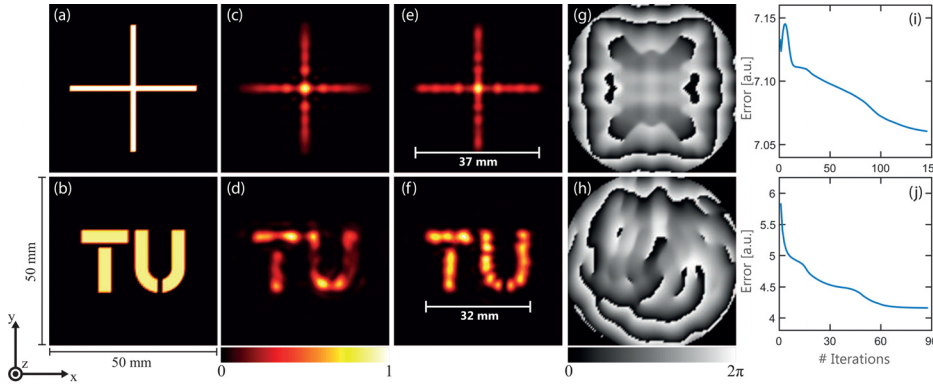
FIG. 1. (a), (b) The target intensity profiles used in present experiments. (c), (d) Calculated intensity profiles at $z_i = 50\,$mm after the first iteration step of the GS algorithm as compared to the result of the last (e), (f) iteration step, respectively. (g), (h) Calculated phase modulation profiles at $z_0 = 0\,$mm. The frames are cropped to $50 \times 50\,$cm^2 size for better comparison with the experiment. (i), (j) Algorithm error (mean square deviation from the target profile) as a function of the iteration number.

$$E^d_{(x,y)}(x',y') = \frac{A_{(x,y)}}{r_{(x,y),(x',y')}} e^{-i\mathbf{kr}_{(x,y),(y',y')}+i\varphi_{(x,y)}},$$

$$E^i_{(x',y')} = \sum_{(x,y)} E^d_{(x,y)}(x',y')[1 + \cos(\Omega)],$$

(1)

where $\mathbf{r}$ represents the vector between the two points on different planes, $\mathbf{k}$ is the wave vector, and Ω is the angle between the normal of the diffraction plane and the vector $\mathbf{r}$. Equation (1) corresponds to the Fresnel-Kirchhoff diffraction formula.[27] Due to the loss of the amplitude information of the optical field profiles during the GS algorithm, the pre-factors in Eq. (1) were left out. Note also that the part in square brackets represents the Fresnel inclination factor.

As the GS algorithm utilizes a subsequent back and forth propagation of the beam, the roles of the image and

diffraction planes at z_i and z_0, respectively, were interchanged in Eq. (1). We note that the reverse propagation requires the change of the sign in the exponent in Eq. (1).

Figures 1(c) and 1(d) show the calculated intensity profiles in the image plane for two targets after the first iteration step of the algorithm. Compared to the results after the final convergence of the algorithm [Figs. 1(e) and 1(f)], which is caused by the calculated beam phase deformation shown in Figs. 1(g) and 1(h) as gray scales, it can be seen that already the first iteration step produces reasonable intensity profiles. It should be noted here that the loss of the 4-fold symmetry of the phase profile in Fig. 1(g) is caused by the incident beam with a rotated asymmetric Gaussian shape described above. The calculated mean square deviations, shown in Figs. 1(i) and 1(j), demonstrate that final convergence of the GS algorithm is reached after about $\sim$100 iterations which take about 4 h of computer time on a commercial laptop. Analyzing the evolution of the errors with increasing iteration steps, we note that the relative improvement is rather small. This fact is due to the large amount of the zero intensity points in the target, which masks the advancement of the image.

Based on the calculated phase profiles shown in Figs. 1(g) and 1(h) as gray scales, two optical elements [presented in Fig. 2(c)], corresponding to the two targets, were modeled by using the formula $z_{(x,y)} = \varphi_{(x,y)}\lambda_0/[(\mathrm{Re}(n) - 1)2\pi]$ to calculate the thickness of the optical elements at transverse positions (x, y) in order to achieve the correct phase-shift profile. The refractive index $n = 1.52 + 005i$ of polylactide (PLA)—the plastic filament of the commercial additive 3D-printer—was measured in a separate experiment at the operating wavelength. This material was used to print the elements using a commercially available 3D-printer with a nozzle diameter of 0.4 mm and spatial resolution of 0.1 mm. We calculated that in the case of the printed phase plates, the complex refractive index n would lead to about 6% of absorption and in addition 5% of reflection at 140 GHz.

The printed elements were positioned into the path of the 140 GHz beam at the z_0-value of the optical system, as shown in Fig. 2(b). The incident beam was produced by an IMPATT diode with 30 mW power. The transverse intensity profile of the phase-modulated optical field behind the phase plates was then measured using a pyroelectric detector on a translator in the xy-plane with a scanning resolution of 0.5 mm and a scanning region size of $50 \times 50\,$mm^2. A sufficient signal-to-noise ratio was achieved by the implementation of a lock-in detection
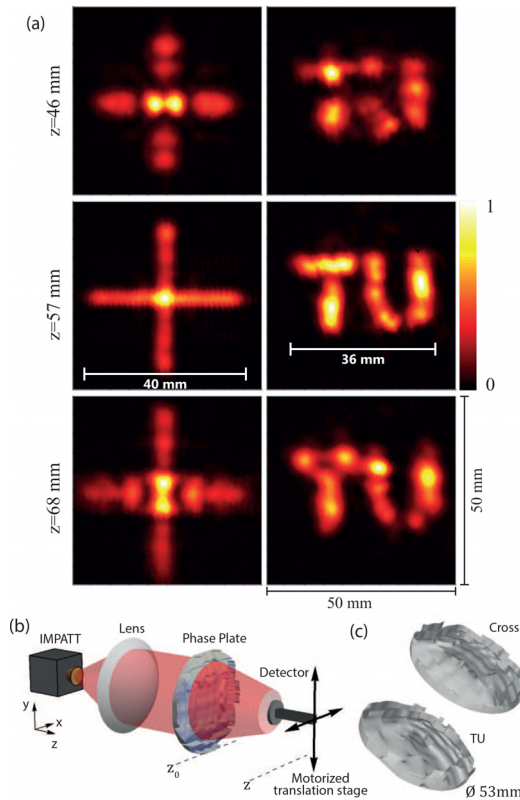

FIG. 2. (a) Experimental intensity profiles of the optical field produced by an incident THz beam that was phase modulated by the two printed elements. The images appeared the sharpest at $z = 57\,$mm. (b) Scheme of the optical setup used for measuring the intensity profiles of the field behind the printed phase plates that were fabricated according to the computer models shown in (c).

system. A sequence of intensity profiles was measured at various positions around the set image plane position z_i. In Fig. 2(a), we present the measured intensity profiles at three different positions z. We found that the sharpest images, which were the closest to the simulated profiles in Figs. 1(e) and 1(f), were located at $z = 57$ mm, slightly deviating from the expected distance of 50 mm. Simultaneously, the effective shape size of the images is also increased compared to respective target images shown in Figs. 1(e) and 1(f) by approximately 10%.

In order to find the reason for the variation of image size, we investigated the influence of the phase distribution of the incident beam. Indeed, in the real experiment, the phase profile of the beam deviates from an ideal plane wave and is better approximated with a spherical beam with a large but yet unknown curvature R. Assuming a finite wavefront radius for the phase part of the optical field of the Gaussian incident beam causes a displacement of the image plane at which the shape of the intensity profile appears the sharpest. In addition, the size of the image increases proportionally to the change in the optimal distance [see Figs. 3(b) and 3(c)].

For each value of R, a set of intensity profiles at various positions z with a step size of $\Delta z = 1$ mm was simulated. From it, we were able to select the position z, at which the shape in the simulated intensity profile appeared focused, for each value of R [see Fig. 3(b)]. Figure 3 also shows that the dependence of image plane position on R coincides with the simple thin lens equation with the focus of z_i (depicted in black), in particular, in the linear regime of the equation $\left(\frac{R}{z_0} \gg 1\right)$. Effective sizes of the sharpest shapes with respect with R, shown in Fig. 3(c), follow the same trend as their positions. This may be expected as a result of a linear

dependence between the image plane position of the sharpest image and its position on the optical axis. For $R = 500$ mm, we see in Fig. 3(b) that the sharpest image appears at $z = 56$ mm, relatively close to the position of the sharpest measured image in Fig. 2(a). In addition, the effective size of the sharpest image for $R = 500$ mm is comparable to the measured one and thus shows that an uncollimated beam with a similar curvature explains well the mismatch of the theoretical prediction and the experimental results, despite our optimization of the optical system.

We also investigated the effect of varying the wavelength of the incoming beam keeping the phase plate fixed the one producing the cross-shaped intensity pattern [see Fig. 1(g)]. Simulated intensity profiles at the image plane z_0 for two wavelengths around the value λ_0 are shown in Fig. 3(a). After comparing these results to Fig. 1(e), we conclude that a noticeable change of wavelength still produces intensity profiles that preserve the basic shape of the target yet it also shows that a specific spectral width of the radiation would influence the sharpness of the image.

We also mention parenthetically that we improved the propagation function in Eq. (1) by better taking into account the finite thickness of the phase plate. Instead of an instant change of the propagation phase (as for a waveplate with zero thickness), a finite height has been added to each emitter of the source plane with a value corresponding to the actual thickness at a point (x,y). This improvement slightly corrected the simulated intensity profiles when compared to real results, yet the changes are barely seen directly and are therefore not shown here.

In conclusion, we demonstrate that versatile wave plates for THz beam shaping can be very easily produced with a commercially available 3D printer. Specifically, we showed how such dielectric phase plates can modulate an incoming Gaussian beam such that it produces an arbitrary image on the detector plane. Our results are expected to facilitate THz imaging on all levels where customized and cost-efficient beam shaping solutions are required.
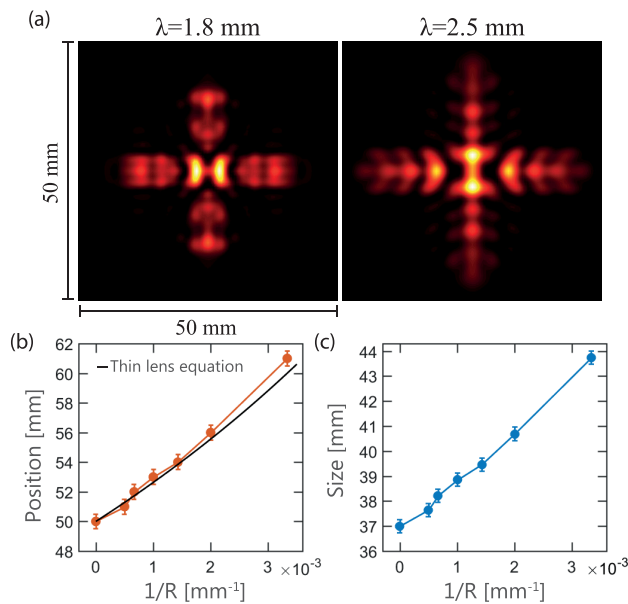
FIG. 3. (a) Simulated intensity profiles of the optical wave function at the image plane, where the wavelength was set to 1.8 and 2.5 mm, respectively, and the incident beam was modulated by the waveplate in Fig. 1(g), optimized for $\lambda = 2.14$ mm. (b), (c) Position and size of the image as a function of the wavefront curvature of the incident beam (R) including the values from Fig. 1, where $R = \infty$. Points mark the results from the simulations, the solid black line represents the thin lens formula with a focus set at $z_i = 50$ mm.

[1]M. Tonouchi, Nat. Photonics **1**, 97 (2007).
[2]C. Jansen, S. Wietzke, O. Peters, M. Scheller, N. Vieweg, M. Salhi, N. Krumbholz, C. Jördens, T. Hochrein, and M. Koch, Appl. Opt. **49**, E48 (2010).
[3]Y. Xing, M. Kaaniche, B. Pesquet-Popescu, and F. Dufaux, *Digital Holographic Data Representation and Compression* (Elsevier Science, 2015).
[4]D. Leseberg, Appl. Opt. **31**, 223 (1992).
[5]K. Matsushima, Appl. Opt. **44**, 4607 (2005).
[6]M. Makowski, M. Sypek, A. Kolodziejczyk, and G. Mikula, Opt. Eng. **44**, 125805 (2005).
[7]M. Makowski, M. Sypek, A. Kolodziejczyk, G. Mikula, and J. Suszek, Opt. Eng. **46**, 045802 (2007).
[8]B. Walther, C. Helgert, C. Rockstuhl, F. Setzpfandt, F. Eilenberger, E.-B. Kley, F. Lederer, A. Tünnermann, and T. Pertsch, Adv. Mater. **24**, 6300 (2012).
[9]J. Sun, E. Timurdogan, A. Yaacobi, E. S. Hosseini, and M. R. Watts, Nature **493**, 195 (2013).
[10]N. Yu and F. Capasso, Nat. Mater. **13**, 139 (2014).
[11]P. Genevet and F. Capasso, Rep. Prog. Phys. **78**, 024401 (2015).

[12]J. Upatnieks and C. Leonard, J. Opt. Soc. Am. **60**, 297 (1970).

[13]M. T. Gale, M. Rossi, H. Schütz, P. Ehbets, H. P. Herzig, and D. Prongué, Appl. Opt. **32**, 2526 (1993).

[14]D. Lin, P. Fan, E. Hasman, and M. L. Brongersma, Science **345**, 298 (2014).

[15]Z. Zeng, H. Zheng, Y. Yu, and A. K. Asundi, Opt. Lasers Eng. **93**, 47 (2017).

[16]S. Rotter and S. Gigan, Rev. Mod. Phys. **89**, 015005 (2017).

[17]S. F. Busch, M. Weidenbach, M. Fey, F. Schäfer, T. Probst, and M. Koch, J. Infrared, Millimeter, Terahertz Waves **35**, 993 (2014).

[18]A. D. Squires, E. Constable, and R. A. Lewis, J. Infrared, Millimeter, Terahertz Waves **36**, 72 (2015).

[19]J. Suszek, A. Siemion, M. S. Bieda, N. Błocki, D. Coquillat, G. Cywiński, E. Czerwińska, M. Doch, A. Kowalczyk, N. Palka *et al.*, IEEE Trans. Terahertz Sci. Technol. **5**, 314 (2015).

[20]A. Hernandez-Serrano, M. Weidenbach, S. Busch, M. Koch, and E. Castro-Camus, J. Opt. Soc. Am. B **33**, 928 (2016).

[21]W. D. Furlan, V. Ferrando, J. A. Monsoriu, P. Zagrajek, E. Czerwińska, and M. Szustakowski, Opt. Lett. **41**, 1748 (2016).

[22]W. J. Otter and S. Lucyszyn, Proc. IEEE **105**, 756 (2017).

[23]A. Hernandez-Serrano and E. Castro-Camus, J. Infrared, Millimeter, Terahertz Waves **38**, 567 (2017).

[24]H. Xin and M. Liang, Proc. IEEE **105**, 737 (2017).

[25]F. Machado, P. Zagrajek, J. A. Monsoriu, and W. D. Furlan, IEEE Trans. Terahertz Sci. Technol. **8**, 140 (2018).

[26]R. W. Gerchberg and W. O. Saxton, Optik **35**, 237 (1972).

[27]M. Born, E. Wolf, A. B. Bhatia, P. C. Clemmow, D. Gabor, A. R. Stokes, A. M. Taylor, P. A. Wayman, and W. L. Wilcock, *Principles of Optics: Electromagnetic Theory of Propagation, Interference and Diffraction of Light*, 7th ed. (Cambridge University Press, 1999).